Capabilities and Limitations of Optical Coherence Tomography as an In-Situ Sensor for Curl and Porosity Detection in Selective Laser Sintering of Nylon 12

A. Lewis, S. Fish, J. Beaman
University of Texas at Austin, USA

Abstract

Despite significant advances made since the inception of selective laser sintering (SLS), many of the same problems identified by early researchers persist today including high part porosity and part resolution limitations. Much of the difficulty in correcting these problems stems from the relative lack of process data available in SLS machines. Because of these issues, part validation and improved process sensors and control continue to be identified as critical areas of improvement in industry roadmaps.
In this paper the utility of optical coherence tomography (OCT) as an in-situ sensor is explored for the SLS process. Specifically, curl is induced in SLS parts during the build process and OCT is used to detect the defect during the build process. Limitations of OCT for curl detection are discussed. Additionally, OCT is found to be able to identify pores within the molten part under some build conditions by comparing OCT data with micro x-ray computed tomography (XCT) data.

1 Inroduction

1.1 Selective Laser Sintering

Additive manufacturing (AM) is a disruptive technology which provides greatly reduced manufacturing times for complex components. Although AM started as a rapid prototyping technology, it is currently transitioning towards becoming a scalable manufacturing technique for end-use parts. Selective Laser Sintering (SLS), one of the earliest commercialized AM technologies, continues to demonstrate rapid growth in recent years. SLS has found increasing use in

industry due to its ability to cost-effectively provide geometrically complex, bespoke polymer parts without the need for support structures [1]. The SLS process is explained using Figure 1 for reference.

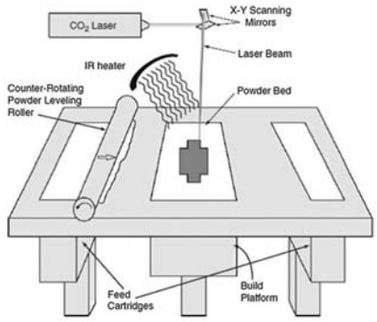

Figure 1: Selective Laser Sintering Process Illustration **[1]**

During the SLS build process, while maintaining the top polymer powder layer (typically around 100μm thick) about 5-10°C below its melting point with infrared heaters, a laser is used to melt select portions of the powder. Next, a new layer of powder is spread on top of the previous layer and the process is repeated until the part is completely formed. It is generally desirable to keep all of the melted material from resolidifying until the entire part can be cooled uniformly in order to minimize thermal stresses and resulting warpage.

Despite significant advances made since the inception of SLS, many of the same problems identified by early researchers including curl and high part porosity persist today [2]. These defects are of particular importance to this paper, and are elaborated upon below.

There are various mechanisms of curl in the SLS process. This paper will deal only with one, which will be called surface curl. This type of curl is described by Goodridge et al. [2] and is summarized here. In the SLS process, if the powder bed temperature is too low, thermal gradients will cause the edges of the sintered area to curl upwards. This curled region is problematic when manufacturing parts with SLS because if the curl is severe enough, the raised region of the part will catch on and be dragged by the powder spreading element as it travels across the powder bed. This prevents subsequent layers from being sintered in the correct positions relative to the dragged, previously sintered layers [2].

Porosity within a part decreases the effective cross section, and in turn decreases the strength of the part. This has been demonstrated by several researchers in SLS parts specifically [3–5]. The ability to detect porosity during a build is an important step towards qualifying the integrity of SLS parts as they are being built as well as researching strategies to reduce or eliminate pores. OCT images are formed as light reflects off of material or phase interfaces in a sample. Pores within a melted nylon region in an SLS part during the build are such an interface, and given a high enough signal, should show up in OCT images.

Much of the difficulty in correcting these defects in the SLS process stem from the relative lack of sensors and feedback control compared to traditional manufacturing techniques. Because of these challenges, quality validation and improved process control continue to be identified as critical areas of improvement in SLS industry roadmaps [6,7]. In response to these needs, optical sensors based on laser interferometry such as Optical Coherence Tomography (OCT) have begun to be researched for their ability to directly measure relevant depth information such as the depth of the melt pool in SLS.

1.2 Optical Coherence Tomography

Optical coherence tomography (OCT) is an established medical imaging technique based on coherence interferometry commonly used in biomedical optics and medicine. OCT data can be used to produce cross-sectional and volumetric images from magnitude and echo time delay data of backscattered radiation. Figure 2 illustrates some of the terminology commonly used in OCT images including in this paper.

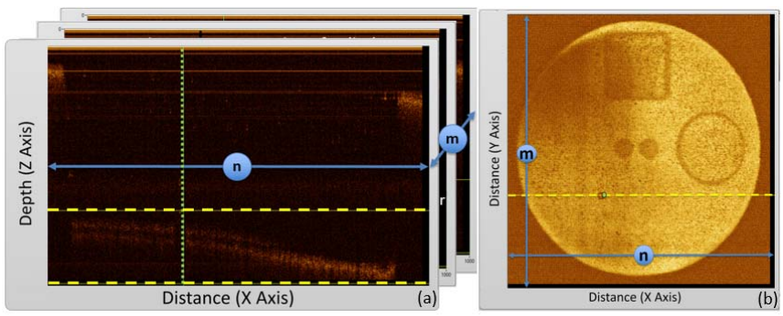

Figure 2: (a) Various B-scans (b) An en face OCT image

A single OCT scan at a point on the surface of the sample is known as an A-scan and yields depth information at this point. The dotted green line is an example of an A-scan, but each vertical column of data in Figure 2(a) is an A-scan. A collection of subsequent A-scans is called a B-scan and yields a cross sectional image of the sample. Each panel in Figure 2(a) shows a B-scan. Subsequent B-scans can be combined to yield a 3D representation of the sample. The backscattered intensity information is typically presented in the false color of B-scans and volumetric renderings. OCT data can also be used to generate a transverse or “en face” image. An en face image can be generated by averaging the pixels corresponding to a certain depth range in each A-scan. The en face image in Figure 2(b) was generated by averaging each column between the yellow dotted lines shown in Figure 2(a) for each of the B-scans. Each A-scan collapsed down to a single pixel and the 3-dimensional dataset consisting of many B-scans collapsed down to a 2D en face image. The data indicated by the yellow dotted line in Figure 2(b) was generated from the B-scan shown at the

front of Figure 2(a). The terms A-scan, B-scan, and en face image are used throughout the paper as described here.

2 Material and Methods

The Laser Additive Manufacturing Pilot System (LAMPS) built at The University of Texas at Austin was the SLS system used for these experiments. The LAMPS machine is comparable to commercial SLS machines in size, but has far superior sensing capabilities including over 40 strip heaters and thermocouples for precise chamber and build box heating, visual and high speed infrared cameras, as well as an OCT system co-aligned with the CO_2 sintering laser. Additional details concerning the LAMPS machine can be found in Fish et al [8]. Additional details concerning how the OCT system is integrated with the LAMPS machine can be found in Gardner et al [9]. All of the powder imaged in this paper was commercially available, virgin PA650 (nylon 12) from Advanced Laser Materials (ALM).

One consequence of the OCT system design is that an artificial curvature is present in the OCT images, especially near the edges of the build surface as described in Gardner et alia [9]. This defect has been corrected in the surface curl portion of this paper by fitting a 2^{nd} order bivariate polynomial to a powder layer, and correcting each surface curl dataset based on that fit. This correction was not necessary on the porosity data since the porosity cylinder part is close to the center of the build chamber and the artificial curvature is very slight there.

Image processing and analysis was performed using FIJI, a distribution of ImageJ [10,11].

3 Results & Discussion

3.1 In Situ Surface Curl Detection

3.1.1 Methods

For this experiment, the powder bed was heated to a temperature on the lower end of the acceptable range of build temperatures in order to be sure to induce surface curl in 3 long thin bars shown in Figure 3(a). On the first and last 15 layers and approximately once every 10 layers during the middle of the build, the build surface was imaged with OCT in the area where the parts were being built. For this build, the powder bed set temperature was 178°C. The laser power at the powder bed surface was 8.8W, with a spot size of 575 μm. The scan speed was 1500 mm/s, and the hatch spacing was 212 μm. The scan lines alternated between +45° and -45° angle each layer. Figure 3(a) shows the geometry of the part which is 165 mm long, 8 mm wide not including the tabs, and 10 mm tall. It is oriented differently from the rest of Figure 3 in order to better show the geometry of the parts.

3.1.2 Results and Discussion

After performing the curvature correction described in Section 2 on the OCT data, curl was easily identified visually on the left side of the part. Figure 3(b) is the en face OCT image of the build surface on layer 10 and shows the three specimen being built. The b-scan located just above the top specimen as indicated by the yellow line is shown in Figure 3(c). Figure 3(c) shows a flat powder surface with a noticeable raised section on the left of the image. This raised portion is surface curl. The area corresponding to the white rectangle is shown for each of the first 15 layers of the build in Figure 3(d). The curl started on the left side of the first layer. The maximum height of the curl grew on each of the first 7 layers after which it began to decrease.

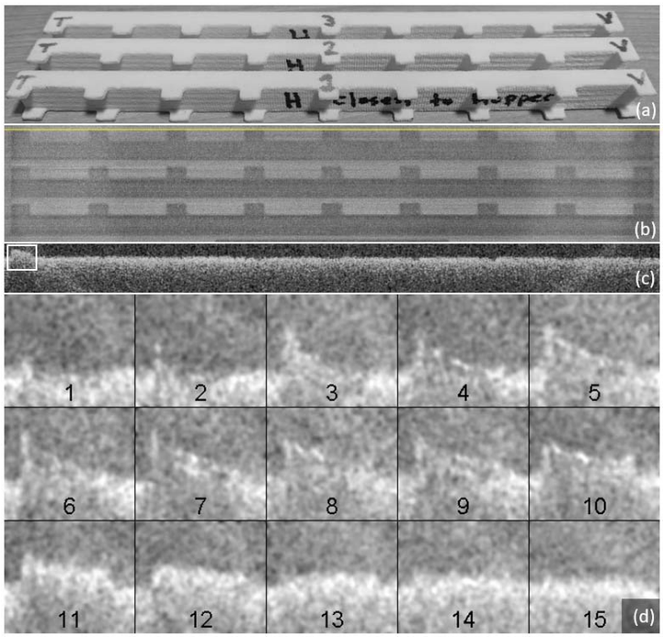

Figure 3: (a) printed parts visual image (b) an en face image of layer 11, (c) a b-scan just above the top part as indicated by the solid line in (b), (d) a montage of the area in the white rectangle of (c) from every dataset for layers 1-15.

It was also possible to plot the height of each area of the entire powder surface on a false color scale. The resulting image looks similar to the en face image, but the useful difference is that the pixel intensity values correspond with the actual height of that region of the build surface. Such a figure is shown in Figure 4(a) and (b).

The following algorithm was used to detect the height of each A-scan in the image. First, the 3D dataset was opened. The average A-scan intensity was calculated then subtracted from each A-scan in the dataset in an attempt to

reduce noise present in the OCT images. A Gaussian blur filter with a radius of 3 pixels was then used to further smooth the effects of noise. The height of each dataset was then corrected as described in Section 2 above. A region of interest (ROI) was selected at the top of the dataset above the powder surface and curl and the noise threshold was determined to be the maximum pixel value in the ROI region in the dataset. The surface of each A-scan was determined to be the first pixel with an intensity above the noise threshold. Any A-scan without a pixel above the noise threshold was set to a null value and not used in further calculations. The height values were then plotted vs. their x-y position. One such height map of layer 10 is shown in Figure 4(a) below. The range of the color scale has been set to emphasize raised areas in white. Figure 4(b) is a montage of the leftmost portion of each height map from layers 1-15. Figure 4(c) is a plot of the average height of the curled subregions from Figure 3(d).

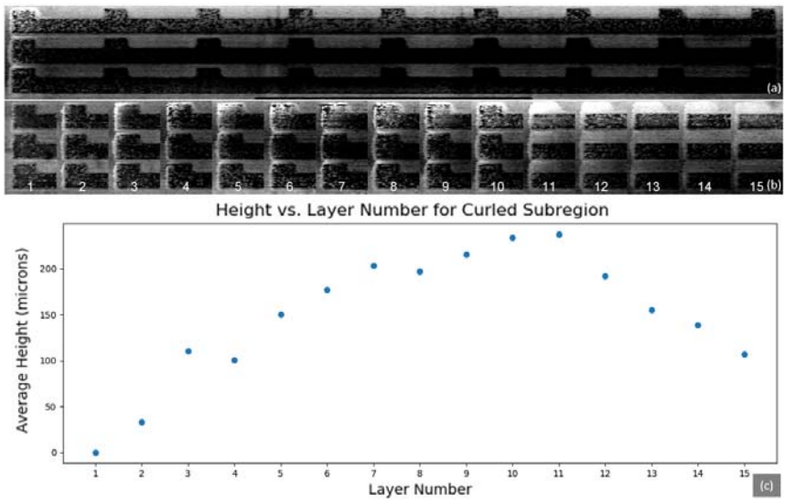

Figure 4: (a) en face image from layer 10 of the build (b) part of the en face image for layers 1-15 (c) plot of average height of the curled subregion vs. layer number

The curl around the top and left edges of the specimen can be clearly seen in Figure 4(a) as regions brighter than neighbouring pixels. Figure 4(b) shows how the curl progresses at each area shown on each layer. The tabs along the top of each specimen are 10 layers thick. Figure 4(b) shows that despite not sintering the powder together in the tab region on layer 11, the powder area in the tab region was still higher than the surrounding areas. This suggests that the cold powder causes curl which is then reduced when the laser melts the powder together and removes voids in the powder. Data such as this suggests raising the set temperature of the heaters which heat the feed powder before it is spread may reduce curl. Figure 4(c) is a plot of the average relative height vs the layer number for the curled sub region shown in Figure 3(d). The data tracked the

increasing curl over the first 11 layers and its decrease thereafter. A common problem in SLS is that curl becomes sufficiently high that the curled part contacts and is dragged by the roller as it spreads new powder, usually resulting in a failed build. Automated generation of data similar to that shown in Figure 3(d) could be used to warn of a build that is likely to fail soon. Quantification of curl in SLS is limited by the axial and lateral resolution of the OCT system being used, about 7.9 and 186 μm respectively. Additionally, using the height detection algorithm mentioned above, the surface was not able to be calculated at every point on the build surface. Scanning for height also extends the build time for each layer by a few seconds since the height scanning is done separately from the sintering scan.

3.2 In Situ Pore Detection

3.2.1 Methods

For this experiment, the powder bed was heated to a temperature of 192°C. A cylinder 30 mm in diameter, and 3 mm in height was built. Several geometric markers were designed on the bottom of the cylinder to facilitate alignment between the OCT and XCT data. The part consists of 5 orientation marking layers and 30 main cylinder layers. The part was imaged with OCT once every 10 layers during the build. The laser power at the powder bed surface was 12.8W, with a spot size of approximately 650μm. The scan speed was 1500mm/s, and the hatch spacing was 279μm. The scan lines alternated between 0° and 90° angle from the x-axis on each layer. An image of the part geometry generated with CAD software is shown in Figure 5 below. The cylinder was then imaged and aligned with XCT as described in Section 2.

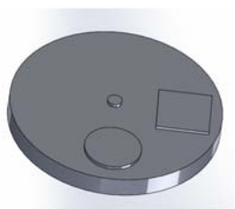

Figure 5: Cylindrical Specimen for Porosity Experiment

3.2.2 Results and Discussion

Figure 6(a) shows a B-scan from the OCT data taken after the final cylinder layer was sintered. Figure 6(b) shows an en face image from the same dataset. The solid lines on the B-scan indicate which depths of the image were used to generate the en face image. The solid line on the en face image indicates which B-scan is being shown in Figure 6(a). The sintered cylinder region is much more transparent in the top several layers than in the surface curl data set in Section 3.1. This is due to the higher build temperature and/or laser power used

in this build versus the surface curl build. A highly scattering layer appears beneath the surface as indicated in Figure 6(a). Based on the depth from the surface, the highly scattering layer is approximately layer 23 of 30 in the build. The highly scattering layer 23 seen here did not extend across the whole cylinder, but was limited to the upper portion of the cylinder as indicated by the bright area of the cylinder in Figure 6(b). Additionally, there are various, small segments of layer 23 which is shadowed by something above it. Figure 6(c) shows a contrast-enhanced, magnified view of the area within the dashed lines from 6(a). In this enhanced image, two bright spots appear above the shadow. This is consistent with a pore which would scatter light at the top and bottom surfaces, and could leave too little focused light to image beneath the pore. This pattern of a shadow beneath two bright spots was seen in many instances in this dataset, though shadows without discernible scatterers above them were also present. This could be explained by insufficient OCT signal being collected to detect some pores in the part. Another notable feature in Figure 6(a) is the curved portion of layer 23. The XCT data shown in Figure 6(d) depicting approximately layer 20 of the cylinder shows a large pore in the same area as the curvature. It's possible that a bubble formed on the surface of the part there, and remained even as powder was spread on top. This may have caused the curvature seen in Figure 6(a) and 6(c) though this data alone is not conclusive.

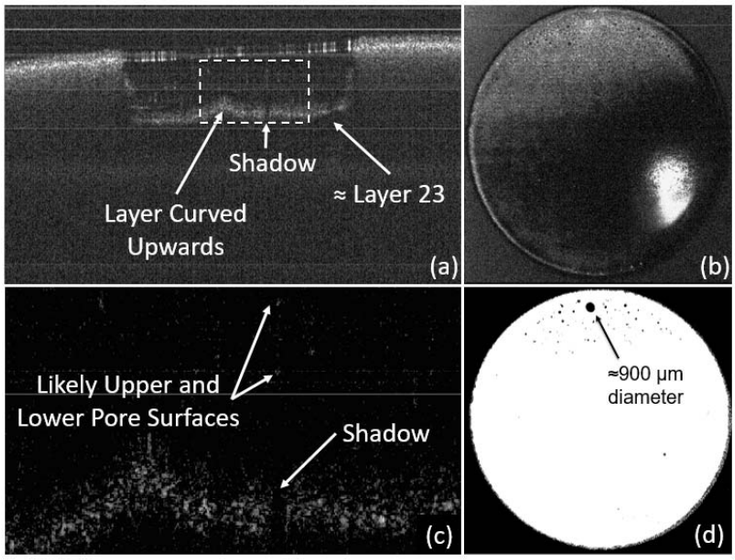

Figure 6: (a)-(c) are OCT images generated from the dataset captured after the last cylinder layer was sintered. (a) A B-scan with several features indicated (b) the en-face image (c) a contrast enhanced, magnified image of (a) is shown (d) XCT cross section showing ≈layer 20

Figure 7(a) shows a cropped, close up of the en face image in Figure 6(b). The data at the depth of the highly scattering layer 23 is used to generate this en-face image. The highly scattering layer was only present on the upper portion of the cylinder so only the upper portion is shown in Figure 7(a). Figure 7(b) shows a cross section from the XCT data showing approximately layer 28 of the cylinder.

There is good agreement between the OCT and XCT data for the larger pores. The en-face OCT image is somewhat noisy, and a standardized pore detection algorithm has not yet been used. Further work is required to detect and calculate the proportion of the large pores which were able to be identified with OCT. Some of the smaller pores seen in the XCT are not visible in the OCT en face image likely due to being smaller than the resolution limit of the OCT system used in these experiments which was approximately 186 µm. For scale, the pore circled in blue in Figure 7 has a diameter of about 260 µm.

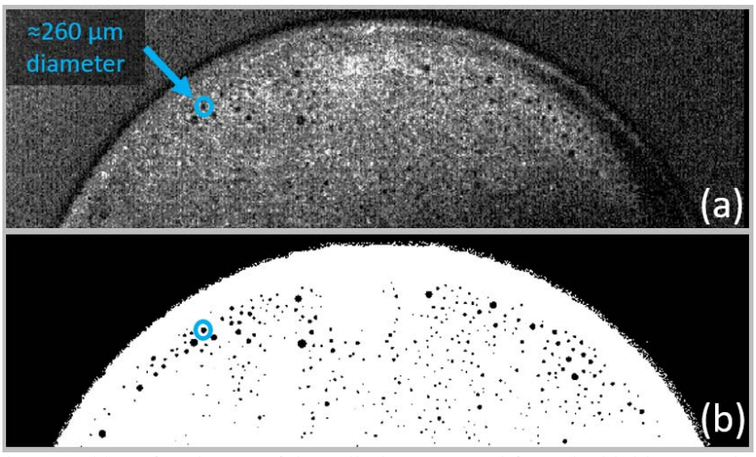

Figure 7: (a) en face image of the cylinder generated from the highly scattering layer depths of the OCT data (b) XCT cross section of approximately layer 28 of the 30 cylindrical build layers

4 Conclusions

In this paper, two SLS builds were performed with different purposes in mind. The first build was performed at a colder build temperature in order to induce surface curl in the part. A height detection algorithm was presented, and various visualizations of the magnitude of the surface curl were presented on layerwise basis from the OCT data including the ability to plot height as a function of layer and location for each imaged location on the build surface.

The second build was performed at a higher powder bed set temperature to attempt to view part porosity during the build. Most layers in the resulting OCT images were much more transparent. Occasionally, a highly scattering layer was

present in the part which prevented imaging below that layer. Pores were shown to cast shadows beneath them, and by generating the en face image based on the highly scattering depths, the pore shadows were compared with the XCT data and good agreement was seen for larger pores on one layer. Additional work would be required to characterize what percentage of pores of what sizes agreed with the XCT data.

References

[1] I. Gibson, D.W. Rosen, B. Stucker, Additive Manufacturing Technologies : Rapid Prototyping to Direct Digital Manufacturing, Springer, Boston, 2009.

[2] R.D. Goodridge, C.J. Tuck, R.J.M. Hague, Laser sintering of polyamides and other polymers, Progress in Materials Science. 57 (2012) 229–267. doi:10.1016/j.pmatsci.2011.04.001.

[3] B. Caulfield, P.E. McHugh, S. Lohfeld, Dependence of mechanical properties of polyamide components on build parameters in the SLS process, JOURNAL OF MATERIALS PROCESSING TECHNOLOGY. 182 (2007) 477–488. doi:10.1016/j.matprotec.2006.09.007.

[4] H.C.H. Ho, I. Gibson, W.L. Cheung, Effects of energy density on morphology and properties of selective laser sintered polycarbonate, Journal of Materials Processing Technology. 89–90 (1999) 204–210. doi:10.1016/S0924-0136(99)00007-2.

[5] A. Wegner, G. Witt, Correlation of Process Parameters and Part Properties in Laser Sintering using Response Surface Modeling, Physics Procedia. 39 (2012) 480–490. doi:10.1016/j.phpro.2012.10.064.

[6] D.L. Bourell, M.C. Leu, D.W. Rosen, Roadmap for Additive Manufacturing: Identifying the Future of Freeform Processing, 2009. https://wohlersassociates.com/roadmap2009A.pdf.

[7] J. Pellegrino, T. Makila, S. McQueen, E. Taylor, Measurement Science Roadmap for Polymer-Based Additive Manfucturing, Energetics Incorporated, 2016. https://doi.org/10.6028/NIST.AMS.100-5.

[8] S. Fish, S. Kubiak, W. Wroe, J. Booth, A. Bryant, J. Beaman, A High Temperature Polymer Selective Laser Sintering Testbed for Controls Research, in: Process Development, Austin, TX, 2015.

[9] M.R. Gardner, A. Lewis, J. Park, A.B. McElroy, A.D. Estrada, S. Fish, J.J. Beaman, T.E. Milner, In situ process monitoring in selective laser sintering using optical coherence tomography, Optical Engineering. 57 (2018) 1. doi:10.1117/1.OE.57.4.041407.

[10] C.A. Schneider, W.S. Rasband, K.W. Eliceiri, NIH Image to ImageJ: 25 years of image analysis, Nature Methods. 9 (2012) 671. doi:10.1038/nmeth.2089.

[11] J. Schindelin, I. Arganda-carreras, E. Frise, V. Kaynig, Fiji: an open-source platform for biological-image analysis, Nature Methods. 9 (2012) 676. doi:10.1038/nmeth.2019.